1980ApJ...239..712S

THE ASTROPHYSICAL JOURNAL, 239:712–724, 1980 July 15
© 1980. The American Astronomical Society. All rights reserved. Printed in U.S.A.

ENERGY SPECTRA OF COSMIC-RAY NUCLEI TO ABOVE 100 GeV PER NUCLEON

M. SIMON,[1] H. SPIEGELHAUER, AND W. K. H. SCHMIDT[2]
Max Planck Institute für Extraterrestrische Physik

AND

F. SIOHAN,[3] J. F. ORMES, V. K. BALASUBRAHMANYAN, AND J. F. ARENS
NASA Goddard Space Flight Center

Received 1979 May 29; accepted 1980 January 28

ABSTRACT

Energy spectra of cosmic-ray nuclei boron to iron have been measured from 2 GeV per nucleon to beyond 100 GeV per nucleon. The data were obtained using an ionization calorimeter flown on a balloon from Palestine, Texas. The 3450 kg payload floated at 7 g cm^{-2} for almost 24 hours. The results are in excellent agreement with those of other workers where overlaps exist. The spectra are not consistent with single power laws, and demonstrate the power of using a single technique sensitive over a large dynamic range. The data are consistent with the leaky box model of cosmic-ray propagation. The boron data indicate that the cosmic-ray escape length decreases with increasing energy as $E^{-(0.4\pm0.1)}$ up to 100 Gev per nucleon. Secondary nuclei from iron are also consistent with this dependence. Predicted changes in the energy dependence of the ratios of primary nuclei O/C and (Fe+Ni)/(C+O) are also observed.

Subject heading: cosmic rays: general

I. INTRODUCTION

All nuclei of the periodic table of the elements are present in the cosmic radiation, and the comparison between the relative abundance of cosmic-ray nuclei and the "universal abundance" provides information about their origin and propagation through interstellar space. Interest in these studies has increased since experimental results indicated that the relative abundance of cosmic-ray nuclei is energy dependent. These results have led to a very lively discussion concerning the understanding of the cosmic-ray confinement mechanisms in the galaxy and interstellar propagation. These observations provide clues in the study of the distribution of path lengths through which the particles pass in the galactic containment region. The mean interstellar matter traversed can be studied by comparing the ratios of the secondary to primary components. Observations show that at high energies the particles traverse less interstellar matter than at low energies, indicating that the cosmic-ray source composition is less subject to corrections at high energies. For this reason much effort has been devoted in the last few years to the development of high energy cosmic ray experiments, and many nuclear species have now been observed at energies up to 100 GeV per nucleon. These results were obtained employing instruments such as ionization spectrometers (Balasubrahmanyan and Ormes 1973; Saito *et al.* 1974; Schmidt *et al.* 1976), gas Cerenkov counters (Juliusson 1974; Caldwell 1977; Lezniak and Webber 1978), and magnetic spectrometers (Orth *et al.* 1978). Based on these data, a variety of interpretations were possible, and there were some differences between different techniques.

In this paper we present the results of the chemical composition of cosmic rays as a function of energy in the range of a few GeV per nucleon to some hundreds of GeV per nucleon for boron through iron. The experiment combined an ionization spectrometer and a gas Cerenkov counter to perform two different and independent energy measurements. This combination also provided for the first time an experimental cross-check on the response of both types of detectors to heavy nuclei.

In all these balloon-borne experiments the major constraint in extending the energy range is the low flux of cosmic ray nuclei at high energies. This requires experiments with large area solid angle factors. In order to maximize the statistical significance of the results, the experiment was optimized for collection area at the expense of both charge and energy resolution. Much of this paper is devoted to a discussion of how the resulting problems are handled so that the critical reader can evaluate these results. A price was paid in terms of the increased background, which had to be evaluated carefully.

The experiment was successfully flown in 1976 October from Palestine, Texas, at a mean altitude of 7 g cm^{-2} residual atmosphere, providing a total exposure of 15.5 m^2 sr hours. The weight of the scientific

[1] Now with University of Siegen, Federal Republic of Germany.

[2] Now with Max Planck Institut fur Aeronomie, Federal Republic of Germany.

[3] NAS/NRC Resident Research Associate, now with Oxford University, England.

© American Astronomical Society • Provided by the NASA Astrophysics Data System

1980ApJ...239..712S

payload was 2653.6 kg and the total suspended payload was 3450 kg.

II. EXPERIMENTAL APPARATUS

A detailed description of the experimental apparatus has been published (Arens *et al.* 1979). Here, a short description of the major components will suffice. Figure 1 shows the experimental configuration. This apparatus consisted basically of three parts: (1) a gas Cerenkov counter on top of the instrument with an energy threshold of 16.5 GeV per nucleon; (2) five organic scintillators (Pilot Y) and a solid Cerenkov counter (Pilot 425) which measured charge and trajectories; and (3) an ionization spectrometer or calorimeter for energy determination.

The sensitive area of the apparatus as defined by the upper scintillator was 1.2 m × 1.2 m, and the geometric factor was 0.72 m^2 sr, which reduced to 0.28 m^2 sr for those particles which penetrated both the gas Cerenkov counter and the spectrometer. For the balloon flight, the instrument was placed in a styrofoam housing for thermal insulation. Because of the large size of the instrument no pressurized gondola was used.

The compromise involved in launching a large payload without a picture device (without a pressurized gondola, no gas filled device such as spark chambers or multiwire proportional counters could be used) created a background problem. Events with a large number of particles, especially those due to air showers at large zenith angles, produced a background which is unusual for experiments of this kind. The method of handling this background will be discussed in § V.

The combination of the gas Cerenkov counter with the ionization spectrometer in this experiment provided a means of cross-checking the response characteristics of both detector systems to heavy nuclei. The response of the ionization spectrometer to the different heavy cosmic-ray nuclei could be calibrated with the threshold and response of the gas Cerenkov counter; the response distribution of the gas Cerenkov counter could be checked for the effects of residual scintillation light by using the spectrometer for energy cuts. These points are discussed in § IV and in more detail in a separate paper (Balasubrahmanyan *et al.* 1980).

The properties and the limitations of the position sensing scintillator technique for determining the trajectories in this high energy cosmic-ray experiment are discussed in the instrument paper (Arens *et al.* 1979). The basic idea behind this technique is simple: one locates the position of incidence by exploiting the fact that the measured signal depends on the location in the scintillator relative to the phototubes. Since the pulse height measurements are subject to photoelectron fluctuations, this technique is most useful for heavy cosmic-ray nuclei. The position of an incident particle could be located to within a few centimeters in the different detectors and was adequate for our purposes; however, the resulting inaccuracy in the trajectories did in fact limit the charge resolution. At high energies the charge resolution was further hampered by backscatter effects, and multiple tracks could not be detected easily, points which will be discussed further.

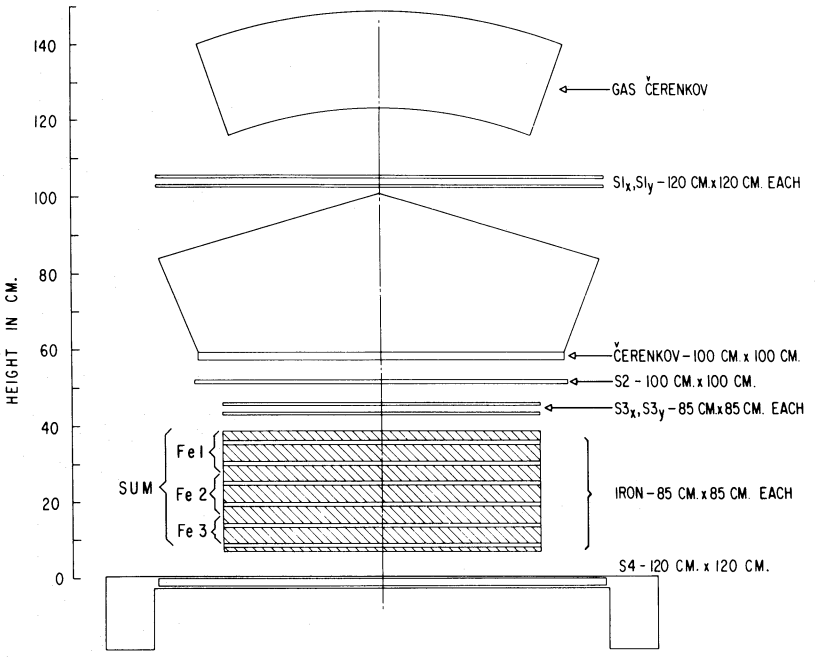

FIG. 1.—Schematic diagram of the German-American high energy cosmic-ray telescope

© American Astronomical Society • Provided by the NASA Astrophysics Data System

1980ApJ...239..712S

III. CHARGE DETERMINATION

The charge determination was performed with five independent charge detectors, i.e., the four scintillators S1x, S1y, S3x, S3y and a solid Cerenkov counter. Since the Cerenkov counter was viewed by two sets, each of four phototubes (PMTs), a total of six charge signals were available. Zenith angle corrections and corrections for the spatial nonuniformity of light collection were applied to all the charge detectors. A series of scatter plots were then constructed from the flight data, in which each scintillator was compared with the Cerenkov response. The curves through the charge peaks in these two dimensional plots, representing the charge lines, were constructed by a best-fit technique. By using all the detectors, a six-dimensional distribution of data and the corresponding charge line was obtained.

An individual cosmic-ray event was attributed to the charge corresponding to the nearest point, measured in units of σ_i, on the charge line, i.e., by minimizing the expression

$$\chi^2 = \sum_{i=1}^{n} \frac{(X_L{}^i - X_p{}^i)^2}{\sigma_i{}^2} . \qquad (1)$$

Here, the $x_L{}^i$ are the coordinates of the position on the charge line to be found, and the $x_p{}^i$ are the charge coordinates of the event considered. The sum extends over all the charge coordinates used, and each term is weighted by the corresponding charge signal variance $\sigma_i{}^2$. The charge variable was thus effectively treated as continuous. The line position was then projected onto the Cerenkov axis for an absolute analog charge measure. The Cerenkov axis was chosen, since no saturation in the signals up to iron nuclei was found, thus yielding a charge measure strictly proportional to Z^2. The above procedure of determining the charge avoided any scale adjustment, since the charge line took into account the individual response of each detector. The absolute value of the minimum χ^2 also provided a measure of the acceptability of an event. Note, however, that this variable is not expected to obey a classical χ^2 distribution because of the non-Gaussian signal fluctuations and a certain degree of correlation among the detector signals.

In the course of the analysis it was observed that the mean pulse height for each charge tended to increase systematically with energy, as illustrated in Figure 2. The rate of signal increase is more pronounced the closer the detector is located to the spectrometer. This behavior is attributed to relatively low-energy particles which flow back from the iron spectrometer. These particles then stop preferentially in the detector close to the spectrometer. The increases in S1x and S1y, the detectors which are further away, are quantitatively consistent with being caused by δ-ray production between 1 and 20 GeV per nucleon (Yodh 1977). Because of the backscatter, only S1x, S1y and the two sets of PMTs from the solid Cerenkov-detector have been used, and the χ^2 values should correspond to three degrees of freedom. Figure 3 shows a charge histogram for χ^2 values between 36 and 100. (A discussion of handling events in the χ^2 range 10–35 is deferred until § V.) The more plentiful species (B, C, O, Ne, Mg, Si, Fe) stand out conspicuously, and the charge resolution is about 0.4 charge units around oxygen and 1.6 charge units around iron. The detector resolution (σ) was about 10% independent of charge and was limited by the accuracy with which the trajectories of an incident particle could be determined. Because individual element resolution has not been

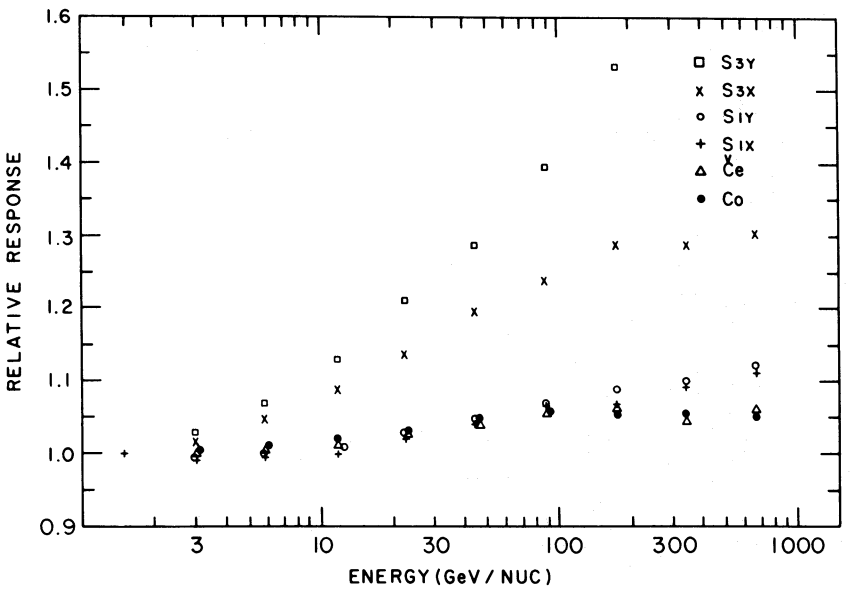

FIG. 2.—Mean response of charge detectors as a function of energy. S_{3x} and S_{3y} are detecting backscattered energy from the calorimeter and hence are not used in the charge analysis.

© American Astronomical Society • Provided by the NASA Astrophysics Data System

1980ApJ...239..712S

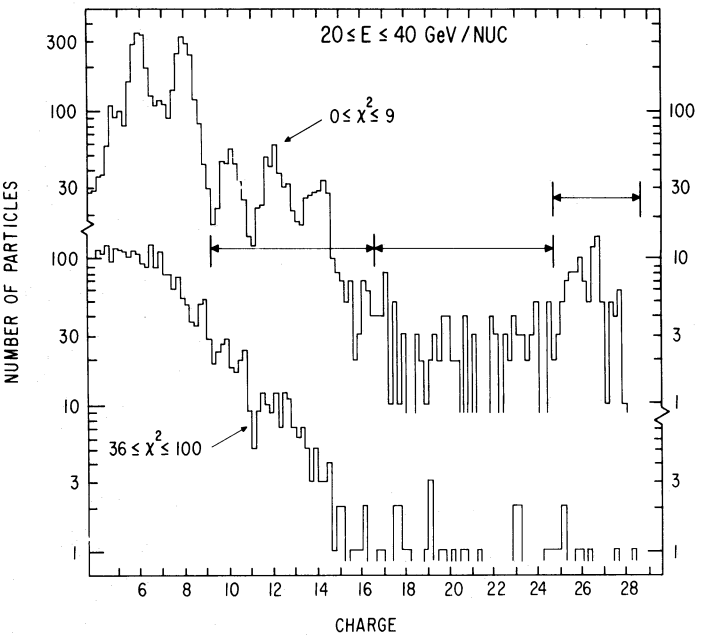

FIG. 3.—Charge histograms for particles between 20 and 40 GeV per nucleon. The upper curve is for good events, and the lower curve is for background events as selected by the consistency of measurements in the charge detectors.

obtained, the elements have been grouped together as indicated in the figure. Because nitrogen lies between the abundant carbon and oxygen and does not clearly stand out, spectra for this nucleus should be considered cautiously. The boron peak appears to stand out in all the plots, and so those results are included. The separation of boron from the abundant background decreases as a function of increasing charge.

The signal resolutions σ_i in equation (1) taken for the four detectors S1x, S1y and the two sets of Cerenkov tubes were, respectively, 7, 5, 7, and 9%. They were obtained by a subset of the carbon and oxygen nuclei which penetrated the central regions of the detectors. We found them to be independent of charge. We assumed that they are independent of energy. This might lead to a slight underestimation of σ at high energies, but as will be shown later, an independent decision is made about the background correction for each charge and energy bin, taking account of any variation. An incident iron nucleus which strips off an alpha particle at the bottom of S1y and hence registers as a chromium in the Cerenkov detector would, in the absence of other fluctuations give a χ^2 value of 9 and lie at the limit of our detection. An iron nucleus that fragments into a calcium nucleus on the other hand, would give a χ^2 value greater than 50 and is easily rejected. An allowance is made for the undetected interactions when the correction is made for interactions in the telescope.

IV. ENERGY DETERMINATION

The principal detector for determining the energy of the cosmic-ray nuclei was the ionization spectrometer (Fig. 1). A primary particle converts a substantial part of its initial kinetic energy into a nuclear electromagnetic cascade. The cascade builds up by a series of nuclear interactions in the spectrometer. Energy is measured by sampling the resultant electromagnetic cascades at various depths in the absorber. In this experiment the iron slab scintillator sandwich was divided into three modules. Each module was viewed from two opposing sides by phototubes at the ends of air light guides with white walls. A vertically incident cosmic ray encounters a total of 170 g cm^{-2} iron plus 5.9 g cm^{-2} scintillator material, which corresponds to 1.44 proton and about six iron nuclear interaction lengths.

For an infinitely deep calorimeter the SUM signal, obtained by summing the scintillator samples from Fe 1, Fe 2, and Fe 3 (see Fig. 1), is proportional to the kinetic energy of the incident nuclei no matter where the first interaction within the calorimeter takes place. All the energy would be absorbed, and the signal distribution would be Gaussian in shape and have a resolution of about 10%. However, in this finite-thickness device, the fraction of the primary energy deposited is dependent upon the location and characteristics of the first interaction, resulting in a broad SUM signal distribution. A thorough discussion concerning this effect on the shape of a measured cosmic-ray spectrum is given in an earlier paper (Jones, Ormes, and Schmidt 1977). In this analysis, in our attempts to improve the resolution, we utilize the fact that the cascade develops differently depending on the location of the first interaction.

The gas Cerenkov counter has been used to provide a calibration for this purpose. Figure 4 shows the

© American Astronomical Society • Provided by the NASA Astrophysics Data System

1980ApJ...239..712S

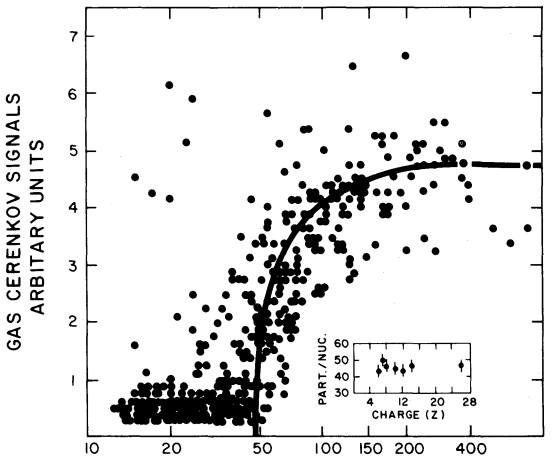

FIG. 4.—A cross plot of the gas Cerenkov detector and the calorimeter for oxygen nuclei (equivalent muons per nucleon). Such plots are used to check the calibration of the calorimeter in the Monte Carlo simulation. The insert shows this calibration for different incident nuclei, confirming its independence of charge.

response of the gas Cerenkov counter for oxygen nuclei as a function of the calorimeter signal. No restrictions have been placed on the calorimeter signals but data have been selected to have trajectories passing through the gas Cerenkov counter and to have consistent signals in the two banks of PMTs. At low calorimeter signal levels the finite response in the gas Cerenkov counter is due to the scintillation in the freon gas. As the energy of particles can be identified in this experiment using the calorimeter, this scintillation level is determined explicitly. Consequently the threshold of the gas Cerenkov counter can be determined quite accurately minimizing the uncertainty due to the scintillation contribution of the gas Cerenkov counter. The curve shown in Figure 4 is based upon the energy determined from equation (2), described below. Similar plots are obtained for other nuclei. From these plots the charge independence of the calorimeter signal (on a per nucleon basis) corresponding to the threshold of the gas Cerenkov counter is demonstrated as seen in the insert in Figure 4.

Plots of the gas Cerenkov response as a function of the calorimeter signal can also be made for given Fe 1 signals. In this manner, the correlation of the calorimeter SUM signal with the Fe 1 signal can be found. This correlation is indicated by the data points in Figure 5. In addition to this experimental check, Monte Carlo simulations (Jones 1976; Jones, Ormes, and Schmidt 1977) have been used to deduce the correlation for other energies. An empirical fit was found which is well represented by the following expression:

$$E = 0.218 \frac{(\mathrm{SUM})^{1.36}}{(\mathrm{Fe\ 1})^{0.38}} \text{ GeV per nucleon} . \qquad (2)$$

The lines in Figure 5 are for constant energy as computed by this formula. The term $\mathrm{SUM}^{1.36}$ has the

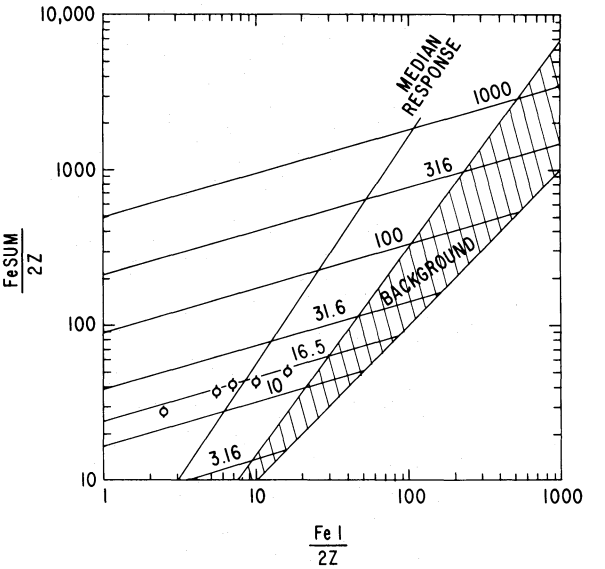

FIG. 5.—This curve shows lines of constant energy on a SUM vs. Fe 1 crossplot. The background region is where events fall which have cascades which develop too fast in the calorimeter. The data points indicate the calibration from the gas Cerenkov threshold based on in-flight oxygen nuclei.

effect of allowing for the increasing fraction of energy escaping out the bottom of the calorimeter as the energy increases, and the term $\mathrm{Fe\ 1}^{-0.38}$ compensates for what happens in the first interaction. Note that when the SUM and Fe 1 signals are expressed in particles per incident nucleon, this expression is independent of charge. The Monte Carlo calculations and the gas Cerenkov data gave consistent values for the constant which represents the energy calibration. Thus, at 16.5 GeV per nucleon our energy scale has been determined to within 5% and is independent of charge. At other energies, since we depend on the Monte Carlo simulation, an increased energy scale error is allowed because of the distance from the gas Cerenkov calibration point. These estimated errors are summarized in Figure 6.

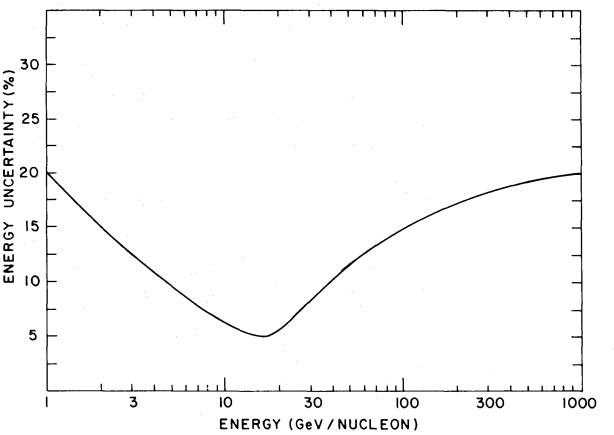

FIG. 6.—The estimated energy uncertainty as a function of energy.

© American Astronomical Society • Provided by the NASA Astrophysics Data System

1980ApJ...239..712S

An example of how equation (2) fits the Monte Carlo simulation is shown in Figure 7 for 100 GeV per nucleon carbon. The clump of particles in the lower left-hand corner of the plot have penetrated deeply into the calorimeter and are lost for energy determination. A correction for this effect is discussed below. The simulations show some Z-dependent effects at low energies (1–3 GeV per nucleon) which may indicate slight problems with the Monte Carlo program at energies where ionization loss effects are important. Therefore only data for energies $E \geq 2.5$ GeV per nucleon are analyzed.

Observed energy distributions for Monte Carlo simulated data are shown in Figure 8. Simulated monoenergetic incident carbon nuclei of 30 GeV per nucleon are analyzed by two different methods. The solid histogram shows the distribution obtained by taking the SUM signal and the dashed histogram shows the improvement obtained by applying the equation (2). The dashed histogram peaks more sharply around 30 GeV per nucleon although both distributions extend to near zero for those particles which penetrated deeply before interacting.

The Monte Carlo events provide a series of distributions which can then be used to deconvolve the energy spectra. Because of the power-law nature of the energy spectra, the slopes are not very sensitive to these deconvolutions. This is true as long as the shape of the response distribution varies slowly with energy (Jones, Ormes, and Schmidt 1977). On the other hand, the intensities must be corrected for the spillage from bin to bin. For example, particles which penetrate deeply into the calorimeter with little or no interaction are lost. They appear as low energy particles, and because of the steeply falling cosmic ray spectrum they have a statistically significant effect only when they fall in the next lower energy bin. Particles which fall into the next higher energy bin are few in number, but their effect is enhanced by the cosmic-ray spectrum. In order to deduce the correct fluxes Monte Carlo simulated distributions for carbon, silicon, and iron, nuclei at 3, 6, 17, 30, and 100 GeV per nucleon were used. Energy bins were overlaid on these plots, and the events lost and those going into adjacent bins were counted. By allowing both for the events lost and gained, appropriately weighted by the spectrum, a correction was derived. Figure 9 shows the multiplicative correction factor $C(\epsilon)$ derived. At low energies, nuclei stop because of ionization loss, so the correction factor is 1, but at higher energies particles can penetrate deeply

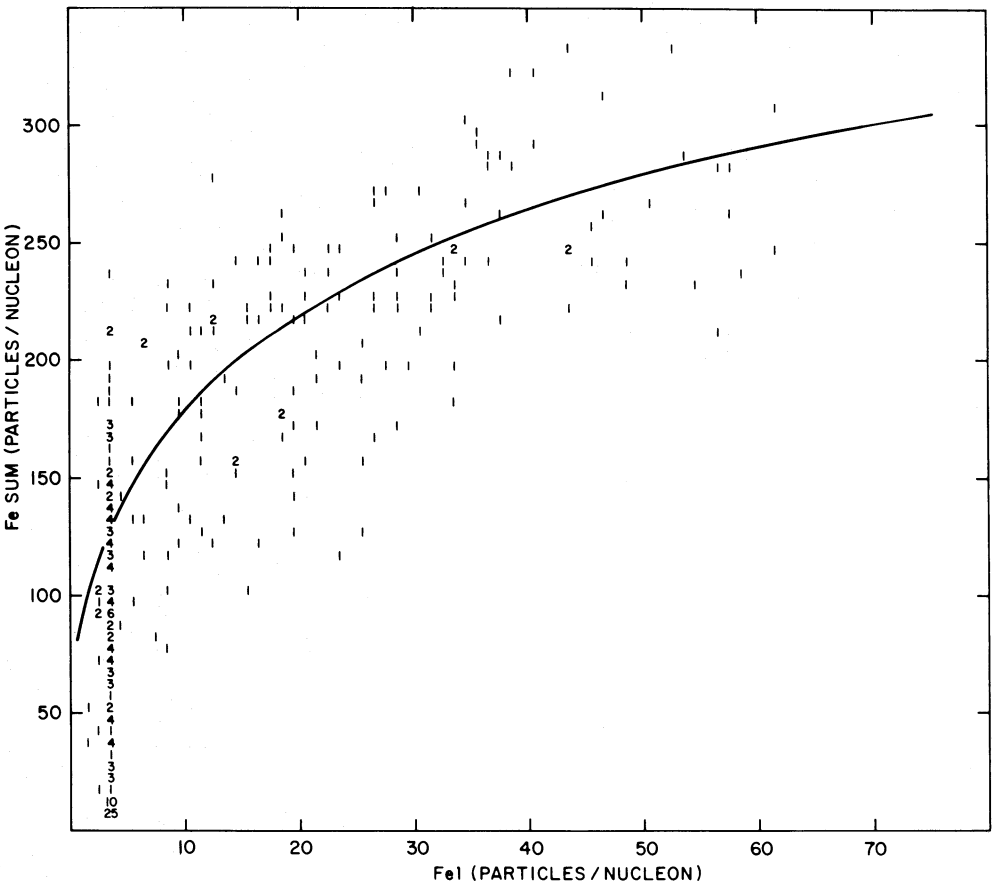

FIG. 7.—Calorimeter response cross plot from the Monte Carlo simulations of 100 GeV per nucleon carbon nuclei. The solid curve represents the calibration curve for 100 GeV per nucleon particles.

© American Astronomical Society • Provided by the NASA Astrophysics Data System

1980ApJ...239..712S

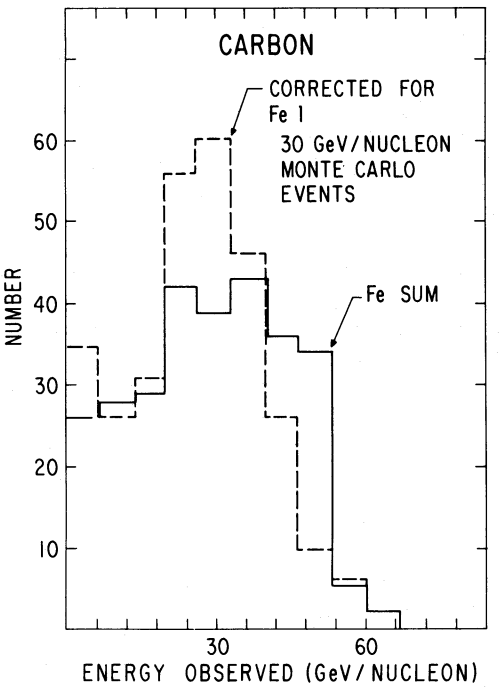

FIG. 8.—The solid curve shows the calorimeter SUM response distribution for 30 GeV per nucleon Monte Carlo simulated carbon events. The dashed curve shows the distribution of observed energies when corrected for the Fe 1 pulse height and the energy escaping out the bottom using equation (2).

either without interacting or by suffering low multiplicity interactions. The net result is a slight flattening of the observed spectra. Uncertainties in these deconvolution corrections are based on the statistical significance of the Monte Carlo runs and are indicated in Figure 9. This error has been included in the quoted flux and dominates at all but the highest energies where statistical errors dominate. In taking ratios of intensities the effect of these convolutions corrections tend to cancel.

V. BACKGROUND

Because of the large area of the experiment and the lack of a trajectory picture device, a substantial background of multiple particles exists, apparently due to air showers, mostly from large zenith angles. Most of these events lie at large χ^2 values (see eq. [1] and the discussion of the charge analysis) indicating that their pulse height were inconsistent in the S1x, S1y and the Cerenkov detectors. However, the low χ^2 tail of the distribution can simulate good events. The background falls off rapidly with increasing charge, but because it has an "apparent" spectrum which is considerably flatter than that of "real" events, is troublesome for low Z particles at high energies. A background event usually gives a trajectory (which measures the "center of gravity" of particles) which is reasonable, and so this cannot be used to reject these events. In summary, the relative amount of background is both charge- and energy-dependent. The method of determining the flux of particles in a given charge and energy bin is illustrated in Figure 10. The open circles indicate the χ^2 distribution for all carbon nuclei in the bin centered at 15.8 GeV per nucleon. Below $\chi^2 = 10$, the distribution is dominated by good events with resolved charges. At high χ^2 (>36) the distributions show no evidence of charge resolution and the distribution is clearly dominated by background. The problem is to determine what to do in the transition where an admixture of background and good events is found and to find an effective cut that properly estimates the background. To do this, a χ^2 distribution consisting predominantly of background was constructed, based upon the shape of the cascades in the calorimeter. For legitimate downward-moving high energy particles, cascades should build up with increasing depth (e.g. Fe 3 signal > Fe 2 > Fe 1). It was observed that events for which this condition was violated had indeed mainly high χ^2 values. Therefore, by selecting events for which a major fraction of the energy was deposited in Fe 1, a χ^2 distribution was formed for background events for

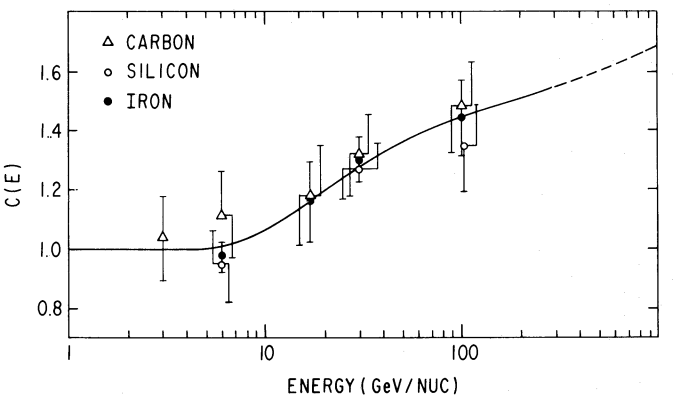

FIG. 9.—Multiplication factors which account for energy bin spillover effects. Primarily these particles have penetrated too deeply in the device to have their observed energy within the resolution bin.

© American Astronomical Society • Provided by the NASA Astrophysics Data System

1980ApJ...239..712S

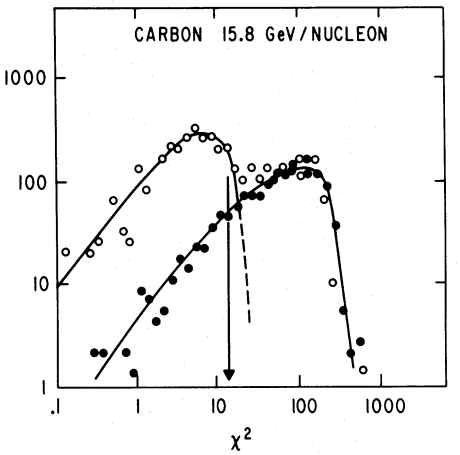

FIG. 10.—An example (15.8 GeV per nucleon carbon nuclei) to illustrate the procedure for subtracting background. The background (*filled circles*) distribution comes from events in the cross hatched region of Fig. 5.

each charge and energy bin. The example, shown in Figure 10 by the solid circles, is typical, and the shapes (for background) were nearly independent of energy. The background distribution is then normalized to the all-particle distribution at large χ^2 values, and the flux of good events is found by a subtraction of two distributions. An effective cut can also be defined which gives the same intensity. At lower energies, the peak-to-valley ratios are pronounced (10:1), and the cuts are obvious and typically occur at χ^2 values of 30. A sequence of examples is shown in Figure 11 for secondary nuclei of boron, carbon, and iron in the energy intervals indicated. The error in this procedure is comparable to the statistical error and has been included in the quoted errors.

VI. INTERACTION CORRECTIONS

A correction is made for the interactions in the 2.57 g cm^{-2} of Al and the 1.28 g cm^{-2} of scintillators at the top of the instrument. The interaction mean-free paths and the corrections used are given in Table 1. The correction factor is adjusted for the fraction of interactions which can be detected by the χ^2 techniques used. For example, in the case of iron secondaries ($17 \leq Z \leq 20$) the correction factor would be 1.43, but since only two-thirds of the interactions are detected, this reduces to $(1 + 2/3 \times 0.43) = 1.29$. The factor 2/3 comes from the partial cross sections for interactions which go undetected, i.e., one in three interacting nuclei do not change charge by enough to raise their χ^2 sufficiently to be rejected.

To correct the fluxes obtained to the top of the atmosphere, a full propagation analysis has been done and growth curves derived. The mean-free paths used are also shown in Table 1. For boron and iron secondary nuclei, a range of values is given, because the correction depends on the abundance ratio (to carbon and iron, respectively) observed; the smaller the observed abundances, the larger the fraction which has been produced in the atmosphere. The quoted errors indicate the range of values used for these data. This correction becomes very important at high energies where the interstellar material traversed is less (at 100 GeV per nucleon ≈ 1 g cm^{-2}), and more than half of the observed flux is atmospherically produced.

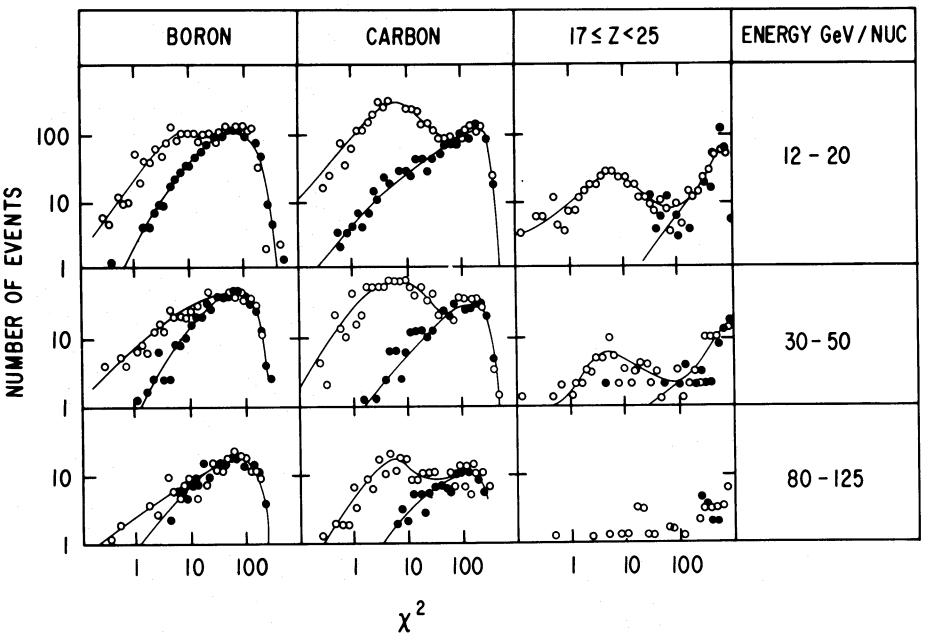

FIG. 11.—Several examples for different charges and energy bins of the χ^2 distributions and the renormalized background distributions. Fluxes are obtained by subtracting these two distributions.

© American Astronomical Society • Provided by the NASA Astrophysics Data System

1980ApJ...239..712S

TABLE 1

INTERACTION LENGTHS AND CORRECTION FACTORS

Charge	MFP[a] in Aluminum	MFP[a] in Scintillator	Correction for Interacting Events Rejected	MFP[a] in Air	Atmospheric[b] Correction	MFP[a] in ISM (10% He)
5	43.2	21.3	1.20	27.5	0.76–0.96	6.6
6	40.1	20.0	1.22	26.2	1.25	6.2
7	37.2	18.6	1.23	24.0	1.22	5.6
8	34.7	17.5	1.26	22.7	1.32	5.1
10	30.8	15.7	1.29	20.8	1.23	4.4
12	27.8	14.4	1.33	10.4	1.34	3.9
14	25.6	13.3	1.36	18.2	1.40	3.52
$10 \leq Z \leq 16$	...	...	1.33	...	1.34	...
$17 \leq Z \leq 20$	...	...	1.29	...	0.86–1.00	...
$21 \leq Z \leq 25$	...	...	1.31	...	0.62–0.93	...
26	19.8	9.3	1.43	13.5	1.44	2.2

[a] MFP = mean-free path for interaction in g cm^{-2}.
[b] At mean slant depth of 7.5 g cm^{-2}.

VII. RESULTS AND CONCLUSIONS

The derived fluxes of all the components at the top of the atmosphere are given in Table 2. Results for oxygen and iron nuclei, multiplied by $E^{2.5}$ power to emphasize the spectral structure, are shown in Figure 12 along with some of the recent data from other groups. The agreement between the different measurements is quite good and generally within the quoted errors. The oxygen data of Lezniak and Webber (1978) seem to be slightly lower than those of the other groups, e.g., the Orth *et al.* (1978) data and those of the Chicago group (Juliusson 1974; Caldwell 1977).

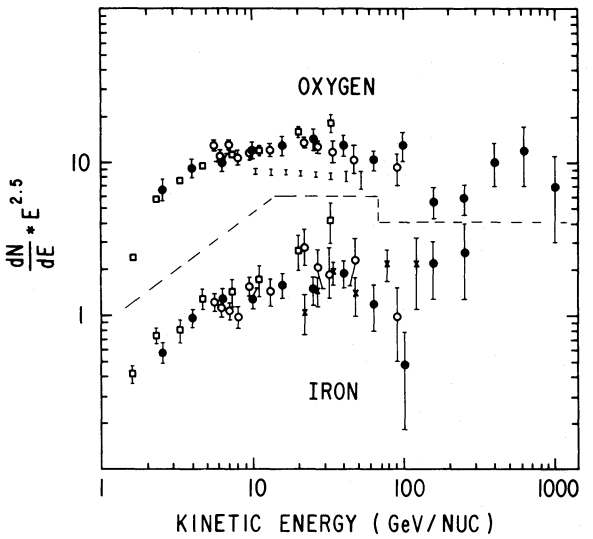

FIG. 12.—The oxygen and iron spectra as determined from this experiment (*solid circles*) compared with measurements of other values. The spectra have been multiplied by $E^{2.5}$ (kinetic energy) to emphasize differences. The intensities are in particles m^{-2} sr GeV per nucleon and kinetic energy is in GeV per nucleon. The open squares refer to Orth *et al.* (1978), the open circles to Caldwell (1977), the crosses to Juliusson (1974), and the vertical lines to Lezniak and Webber (1978).

The spectra derived from this experiment are shown in Figure 13, again multiplied by $E_K^{2.5}$ power. The spectra are given as functions of kinetic energy. The oxygen data span almost three decades in energy (corresponding to seven decades in intensity). The low energy data (2–20 GeV per nucleon), when plotted as a function of total energy $\times E_T^{2.5}$, are quite flat; but the data at high energy indicate that there is a gradual steepening of the spectra. For example, between 2 and 20 GeV per nucleon the iron data are fitted by $E_K^{-2.2}$, while the highest energy data are consistent with $E_K^{-2.7}$. The results agree with spectra derived using a thicker calorimeter (Balasubrahmanyan and Ormes 1973) and with gas Cerenkov counters (Juliusson 1974; Caldwell 1977) when allowance is made for the different energy coverage of the different experiments. It should be noted that the statistics are not sufficient to rule out the iron spectrum which Goodman *et al.* (1979) require to explain their observations of delayed particles at mountain altitudes. Their results at 2–20 TeV per nucleon indicate an iron spectrum as flat as $E^{-2.36\pm0.06}$ from 10 GeV per nucleon onward.

In Figure 14 the experimental B/C + O ratio is shown along with the best fit power-law dependence of the mean escape length,

$$\lambda_e = 9 \text{ g cm}^{-2}(E/\text{GeV per nucleon})^{-(0.4\pm0.1)} .$$

The calculation is based upon an exponential distribution of vacuum path lengths in the phenomenological leaky box model for cosmic-ray propagation. The interaction mean free paths used for the propagation calculation, including the effect of 10% He, are given in the last column of Table 1. (See Ormes and Freier [1978] and references therein for a discussion of the propagation model). The partial cross sections are calculated using the semiempirical formulae of Silberberg and Tsao (1973, 1977). This mean escape length has been allowed to vary with energy in the manner indicated in order to fit to the data in the

© American Astronomical Society • Provided by the NASA Astrophysics Data System

© American Astronomical Society • Provided by the NASA Astrophysics Data System

1980ApJ...239..712S

TABLE 2

FLUXES IN PARTICLES (m^2 sr s GeV per nucleon)

$(X \pm \Delta X) - N \equiv (X \pm \Delta X) \times 10^{-N}$

Energy (GeV/Nucleon)	Boron	Carbon	Nitrogen	Oxygen	$10 \leq Z \leq 16$	$17 \leq Z \leq 20$	$21 \leq Z \leq 25$	$26 \leq Z \leq 30$
2.5	0.17 ± 0.03	0.68 ± 0.1	0.25 ± 0.04	0.66 ± 0.09	0.48 ± 0.07	$(2.6 \pm 0.4) - 2$	$(1.5 \pm 0.3) - 2$	$(5.8 \pm 0.9) - 2$
4.0	$(7.7 \pm 1.2) - 2$	0.27 ± 0.04	0.11 ± 0.02	0.29 ± 0.04	0.22 ± 0.03	$(1.2 \pm 0.2) - 2$	$(8.2 \pm 1.3) - 3$	$(3.0 \pm 0.4) - 2$
6.3	$(2.0 \pm 0.3) - 2$	$(9.4 \pm 1.4) - 2$	$(3.4 \pm 0.5) - 2$	0.10 ± 0.013	$(7.9 \pm 1.2) - 2$	$(4.5 \pm 0.7) - 3$	$(3.0 \pm 0.5) - 3$	$(1.3 \pm 0.2) - 2$
10.0	$(5.6 \pm 0.1) - 3$	$(3.5 \pm 0.5) - 2$	$(1.2 \pm 0.2) - 2$	$(3.8 \pm 0.5) - 2$	$(2.8 \pm 0.4) - 2$	$(1.7 \pm 0.3) - 3$	$(1.0 \pm 0.2) - 3$	$(4.2 \pm 0.7) - 3$
16.0	$(1.8 \pm 0.3) - 3$	$(1.2 \pm 0.2) - 2$	$(3.7 \pm 0.6) - 3$	$(1.3 \pm 0.2) - 2$	$(0.99 \pm 0.15) - 2$	$(5.0 \pm 0.8) - 4$	$(3.5 \pm 0.6) - 4$	$(1.6 \pm 0.3) - 3$
25.0	$(7.9 \pm 1.2) - 4$	$(3.7 \pm 0.5) - 3$	$(1.1 \pm 0.2) - 3$	$(4.5 \pm 0.7) - 3$	$(2.9 \pm 0.4) - 3$	$(1.4 \pm 0.3) - 4$	$(1.1 \pm 0.2) - 4$	$(4.8 \pm 0.9) - 4$
40.0	$(1.5 \pm 0.5) - 4$	$(1.1 \pm 0.2) - 3$	$(2.7 \pm 0.5) - 4$	$(1.3 \pm 0.2) - 3$	$(0.95 \pm 0.15) - 3$	$(5.3 \pm 1.1) - 5$	$(3.7 \pm 0.8) - 5$	$(1.9 \pm 0.4) - 4$
63.0	$(4.0 \pm 1.4) - 5$	$(2.5 \pm 0.5) - 4$	$(7.4 \pm 2.0) - 5$	$(3.3 \pm 0.5) - 4$	$(3.0 \pm 0.5) - 4$	$(1.2 \pm 0.4) - 5$	$(1.0 \pm 0.3) - 5$	$(3.9 \pm 1.2) - 5$
100.0	$(1 \pm 0.4) - 5$	$(8.0 \pm 0.1) - 5$	$(1.8 \pm 0.6) - 5$	$(1.3 \pm 0.3) - 4$	$(0.91 \pm 0.2) - 4$	$(6.5 \pm 2.3) - 6$	$(2.7 \pm 1.1) - 6$	$(4.6 \pm 3.0) - 6$
160.0	...	$(2.9 \pm 0.4) - 5$	$(3.9 \pm 2.0) - 6$	$(1.8 \pm 0.4) - 5$	$(2.4 \pm 0.5) - 5$	$(1.3 \pm 0.8) - 6$	$(7.6 \pm 4) - 7$	$(6.9 \pm 3) - 6$
250.0	...	$(4.4 \pm 1.3) - 6$	$(4.0 \pm 4) - 7$	$(5.9 \pm 1.3) - 6$	$(0.81 \pm 0.2) - 5$	...	...	$(2.6 \pm 2) - 6$
400.0	...	$(1.8 \pm 0.8) - 6$	...	$(3.2 \pm 1.0) - 6$	$(1.7 \pm 0.7) - 6$	...	...	...
630.0	...	$(6.1 \pm 0.4) - 7$	...	$(1.2 \pm 0.5) - 6$	$(5.4 \pm 3) - 7$	...	...	...
1000.0	...	...	...	$(2.2 \pm 1.3) - 7$	$(1.2 \pm 1.2) - 7$	...	...	...

1980ApJ...239..712S

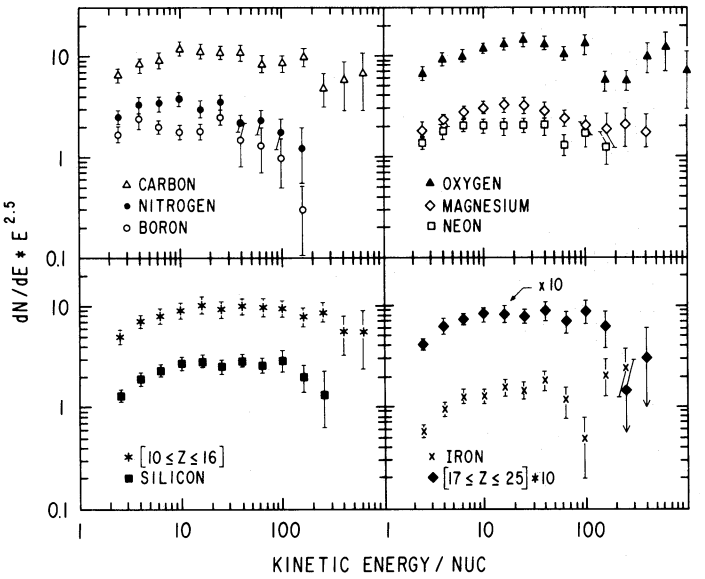

FIG. 13.—The spectra of various components as determined from this experiment multiplied by $E^{2.5}$ (kinetic energy) to emphasize spectral features. The intensities are in particles m^2 sr GeV per nucleon and kinetic energy is in GeV per nucleon.

energy range of this experiment. This energy dependence of the mean escape length is consistent within errors of those previously derived (Caldwell 1977; Lezniak and Webber 1978; Orth *et al.* 1978). Because of the competition between escape and interaction loss mechanisms, ratios between primary nuclei also vary in this model. In Figures 15 and 16 the O/C and the (Fe+Ni)/(C+O) ratios are shown, again compared with the expected ratios as a function of energy. The λ_e has the same form as fitted to the B/C+O data, and the source ratios are taken from Shapiro, Silberberg, and Tsao (1975). A 10% higher source abundance of O would fit the O/C ratio and the (Fe+Ni)/C+O) ratios better. The larger source ratio of iron derived by Lezniak and Webber (1978) is not indicated by these data.

Finally in Figure 17 the ratio of iron secondary nuclei ($17 \leq Z \leq 25$) to iron nuclei is shown along with the results from other workers. Our high-energy data tend to fall below the predicted ratios, especially in the energy range 3–30 GeV per nucleon. The predicted ratios have been calculated based upon a cross section for fragmentation of iron into ($21 \leq Z < 25$) of 411 mbar. The higher ratio observed around 1 GeV per nucleon by Lezniak and Webber (1978) probably reflects the increase in the cross section toward lower energy. The subiron nuclei can be used to probe the shape of the cosmic-ray path length distribution.

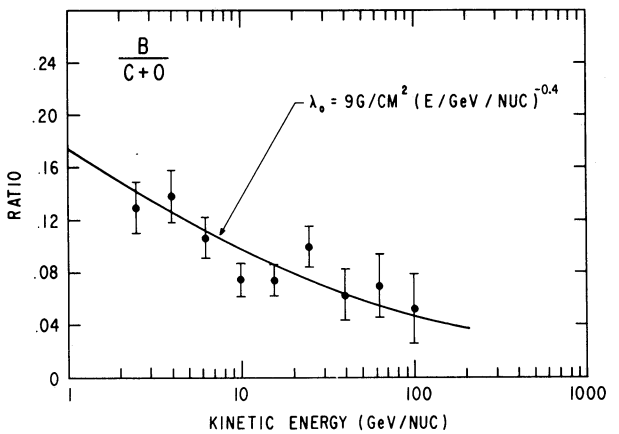

FIG. 14.—The B/(C+O) from these measurements compared to mean escape lengths calculated as a function of the energy dependence indicated.

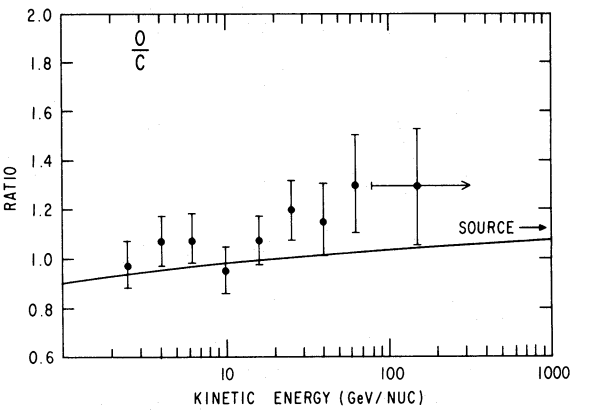

FIG. 15.—The same calculation (see Fig. 14) compared to the O/C ratio data. The source ratios are taken from Shapiro *et al.* (1975).

© American Astronomical Society • Provided by the NASA Astrophysics Data System

1980ApJ...239..712S

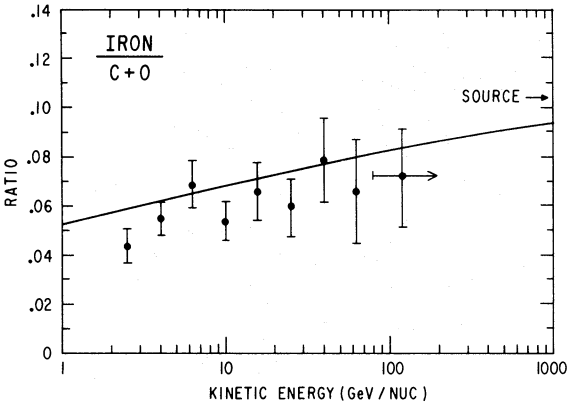

FIG. 16.—The same calculation (see Fig. 14) applied to the (Fe + Ni)/(C + O) ratio data.

Various workers (Lezniak and Webber 1980; Garcia-Munoz, Mason, and Simpson 1977) studying cosmic rays below 1 GeV per nucleon have suggested that the subiron abundances are large enough that the path length distribution must be truncated below 1 g cm^{-2} (Shapiro, Silberberg, and Tsao 1973). Since the cross sections and especially their energy dependence in the range 1–10 GeV per nucleon are not adequately known, it is difficult to draw any conclusions about the cosmic-ray path length distribution based upon these data. However, since truncation of the cosmic-ray path length distribution will increase the number of secondary iron nuclei predicted, it is difficult to see how our data can be consistent with any truncation. Further measurements of the cosmic-ray intensity above the atmosphere and better determination of the energy dependence of the cross sections of the energy range 1–10 GeV per nucleon will be required to resolve this question.

In conclusion, the data are all consistent with a quite simple propagation model in which the escape of cosmic rays from the galaxy is energy dependent. At high energies (>50 GeV per nucleon) the uncertainties in the atmospheric corrections are important and indicate the need for satellite measurements. At around 100 GeV per nucleon the cosmic rays observed at Earth are almost an order of magnitude younger than those at 1 GeV per nucleon and more nearly reflect the source composition. When high statistics observations of the nuclei in the charge range $9 \leq Z \leq 25$ are made above the atmosphere at 100 GeV per nucleon the source composition of these rare components can be determined.

We thank Dr. F. B. McDonald and Dr. K. Pinkau for their support and encouragement. C. R. Greer, G. Cooper, and A. Puig helped to build and test the detectors under the able supervision of J. Laws who provided electrical engineering support. This experiment was also supported by the Bundesminister für Forschung and Technologie of Federal Republic of Germany under the title WRK244 and WRK275:5. Also, thanks, are due to the excellent launch and support provided by the crew of the National Scientific Balloon Facility at Palestine, Texas for launching this payload, which set a record for weight carried above 100,000 feet on a balloon.

We also thank an anonymous referee for carefully reading the manuscript and providing us with several helpful suggestions.

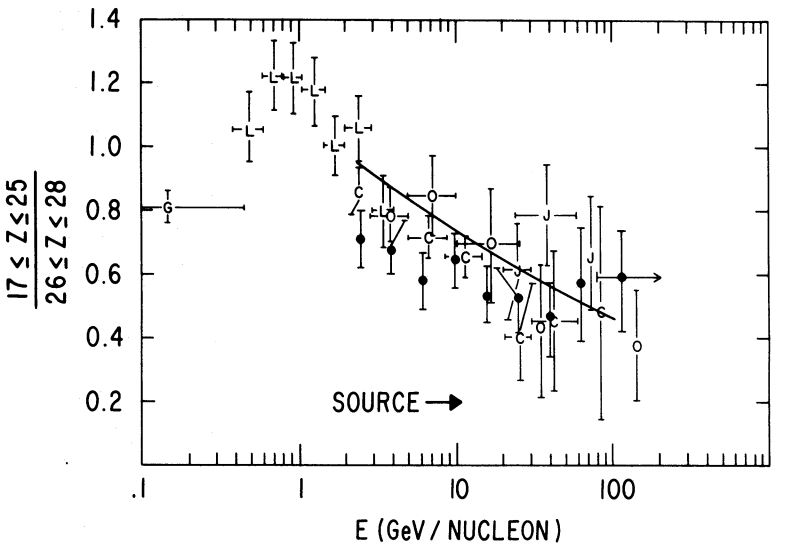

FIG. 17.—The ratio of iron secondary nuclei to iron nuclei compared to the data of other workers. The symbols are as follows: G stands for Garcia-Munoz, Mason and Simpson (1977); L for Lezniak and Webber (1978); C for Caldwell (1977); J for Juliusson (1974); O for Orth *et al.* (1978); and solid symbols represent this work.

© American Astronomical Society • Provided by the NASA Astrophysics Data System

1980ApJ...239..712S

REFERENCES

Arens, J. F., Balasubrahmanyan, V. K., Ormes, J. F., Siohan, F., Schmidt, W. K. H., Simon, M., and Spiegelhauer, H. 1979, *Space Science Instr.*, **4**, 303.

Balasubrahmanyan, V. K., Arens, J. F., Ormes, J. F., Siohan, F., Yodh, G. B., Simon, M., and Spiegelhauer, H. 1980, *Ap. Space Sci.*, in press.

Balasubrahmanyan, V. K., and Ormes, J. F. 1973, *Ap. J.*, **186**, 109.

Caldwell, J. H., 1977, *Ap. J.*, **218**, 269.

Garcia-Munoz, M., Mason, G. M., and Simpson, J. A. 1977, *Proc. 15th Intl. Cosmic-Ray Conf.*, Plovdiv, **1**, 224.

Goodman, J. A., *et al.* 1979, *Phys. Rev. Letters*, **42**, 854.

Jones, W. V. 1976, *Nuclear-Electromagnetic Cascade Monte-Carlo Simulation Program*, GSFC internal memo.

Jones, W. V., Ormes, J. F., and Schmidt, W. K. H. 1977, *Nucl. Inst. Methods*, **140**, 557.

Juliusson, E. 1974, *Ap. J.*, **191**, 331.

Lezniak, J. A., and Webber, W. R., 1978, *Ap. J.* **233**, 676.

———. 1980, *Ap. J.*, in press.

Ormes, J. F., and Freier, P. S., 1978, *Ap. J.*, **222**, 471.

Orth, C. D., Buffington, A., Smoot, G. F., and Mast, T. S. 1978, *Ap. J.*, **226**, 1147.

Saito, T., Sato, A., Sugimoto, H., Matsubayashi, T., and Noma, M. 1974, *J. Phys. Soc. Japan*, **37**, 1462.

Schmidt, W. K. H., Atallah, K., Cleghorn, J. F., Jones, W. V., Modlinger, A., and Simon, M. 1976, *Astr. Ap.*, **46**, 49.

Shapiro, M. M., Silberberg, R., and Tsao, C. H. 1973, *13th Intl. Cosmic-Ray Conf.*, Denver, **1**, 578.

———. 1975, *14th Intl. Cosmic-Ray Conf., Munich*, **2**, 532.

Silberberg, R., and Tsao, C. H. 1973, *Ap. J. Suppl.*, **25**, 315; **25**, 335.

———. 1977, *Proc. 15th Intl. Cosmic-Ray Conf.*, Plovdiv, **2**, 84; **2**, 89.

Yodh, G. B. 1977, private communication.

J. F. ARENS: Code 690, NASA Goddard Space Flight Center, Greenbelt, MD 20771

J. F. ORMES and V. K. BALASUBRAHMANYAN: Code 661, NASA Goddard Space Flight Center, Greenbelt, MD 20771

W. K. SCHMIDT: Max-Planck-Institut für Aeronomie, 3411 Katlenburg-Lindau 3, Federal Republic of Germany

MANFRED SIMON: University of Siegen, Federal Republic of Germany

F. SIOHAN: Oxford University, Oxford, England

H. SPIEGELHAUER: Max Planck Institut für Extraterrestrische Physik, 8046 Garching, Federal Republic of Germany

© American Astronomical Society • Provided by the NASA Astrophysics Data System